

Simulation-based inference of black hole ringdowns in the time domain

Costantino Pacilio^{1,2,*}, Swetha Bhagwat³, and Roberto Cotesta⁴

¹*Dipartimento di Fisica “G. Occhialini”, Università degli Studi di Milano-Bicocca, Piazza della Scienza 3, 20126 Milano, Italy*

²*INFN, Sezione di Milano-Bicocca, Piazza della Scienza 3, 20126 Milano, Italy*

³*School of Physics and Astronomy & Institute for Gravitational Wave Astronomy, University of Birmingham, Birmingham, B15 2TT, United Kingdom*

⁴*William H. Miller III Department of Physics and Astronomy, Johns Hopkins University, 3400 N. Charles Street, Baltimore, Maryland, 21218, USA*

(Dated: December 4, 2024)

Gravitational waves emitted by a ringing black hole allow us to perform precision tests of general relativity in the strong field regime. With improvements to our current gravitational wave detectors and upcoming next-generation detectors, developing likelihood-free parameter inference infrastructure is critical as we will face complications like nonstandard noise properties, partial data and incomplete signal modeling that may not allow for an analytically tractable likelihood function. In this work, we present a proof-of-concept strategy to perform likelihood-free Bayesian inference on ringdown gravitational waves using simulation based inference. Specifically, our method is based on truncated sequential neural posterior estimation, which trains a neural density estimator of the posterior for a specific observed data segment. We setup the ringdown parameter estimation directly in the time domain. We show that the parameter estimation results obtained using our trained networks are in agreement with well-established Markov-chain methods for simulated injections as well as analysis on real detector data corresponding to GW150914. Additionally, to assess our approach’s internal consistency, we show that the density estimators pass a Bayesian coverage test.

I. INTRODUCTION

The detection of gravitational waves (GWs) from binary black-hole (BBH) mergers [1] enables the possibility to perform novel tests of general relativity (GR) in the strong-field regime [2–4]. GR predicts that stationary black holes (BHs) are described by a strikingly simple two-parameter family metric known as the Kerr solution [5], a result that is commonly known as the “no-hair theorem” [6, 7]. This is particularly relevant to the final phase of a BBH evolution, where the two black holes have merged to form a perturbed remnant that settles down to a stationary Kerr BH [8].

Perturbed BHs shed away multiple moments by emitting GWs [9] with characteristic complex oscillation frequencies called quasinormal modes (QNMs) [10, 11]. In GR, the oscillation frequency spectrum can be predicted from the mass and spin of the remnant BH [11, 12] in accordance with the no-hair theorem. Detecting multiple QNMs from the observed signal, also known as black-hole spectroscopy [13, 14], allows us to test deviations from the BH geometry and in the perturbative equation of motion in GR as well as the boundary conditions imposed to solve the perturbative equation of motion [15, 16].

Detecting multiple QNMs unambiguously with present GW detectors has been challenging thus far due to the low signal-to-noise ratio (SNR) in the ringdown portion of the signal [3, 4, 14] (but see [17, 18] for recent hints of multiple QNMs detections from GW data). On the other hand, it is expected that multiple ringdowns at high SNRs will be observed with next-generation GW

detectors such as LISA [19], Einstein Telescope [20], and Cosmic Explorer [21].

Next-generation detectors are expected to routinely observe ringdown SNRs as high as $\mathcal{O}(100)$, with exceptionally loud events having SNRs greater than 1000 [22–26]. Such observations will enable to detect several superimposed QNMs and measure deviations from GR at subpercent level [25, 26]. These will require more powerful Bayesian techniques to both isolate the signal from the background noise and to handle nonstandard noise properties like nonstationarities and non-Gaussianities [27–29], and gaps in data as well as systematics in modeling the signal [30]. Hence, exploring alternative inference methods is of fundamental interest.

The aim of this paper is to propose a likelihood-free method for the parameter estimation of BH ringdowns, based on simulation-based inference (SBI) [31]. SBI methods have been previously applied to GW inference of a full inspiral-merger-ringdown signals, starting with the pioneering works of [32–35] and followed by manifold improvements [36–39]. All these studies show that SBI reaches an accuracy comparable with traditional Markov-chain methods for a full inspiral-merger-ringdown waveform [40–43] and also allow for a considerable speedup in the analysis.

In addition, SBI is highly efficient in estimating automatically marginalized posterior densities [39]. This is crucial in the parameter estimation of BHs in the ringdown phase when the observable signal includes a very large number of QNMs but, in practice, one is only interested in a small subset of well-resolved modes for testing GR purposes [44–47].

In this work we introduce a time domain implementation of likelihood-free inference of BH ringdowns using SBI.

* costantino.pacilio@unimib.it

In contrast to frequency domain approaches presented in a recent study [48], this technique facilitates noise simulation and requires fewer training samples. Likelihood-free ringdown inference in the time domain was first explored in [49] based on the technique of conditional variational autoencoders [50, 51]. Here, we demonstrate for the first time that SBI matches the performance of well-established Markov-chain methods for several simulated signal injections [52, 53]. We also provide a real-data application of estimating the posterior mass and spin of the final BH remnant from GW150914 [1], which agrees well with previous Bayesian analyses [54].

II. SEQUENTIAL NEURAL POSTERIOR ESTIMATION

We use sequential neural posterior estimation (SNPE) to estimate posterior densities. SNPE was first introduced in [55] and further expanded in [56, 57]. The aim of SNPE is to train an approximate density estimator $q_\phi(\boldsymbol{\theta}|\mathbf{x})$ of the true posterior density $p(\boldsymbol{\theta}|\mathbf{x})$. Here, \mathbf{x} is the data segment and $\boldsymbol{\theta}$ is the set of model parameters to be estimated; in particular, \mathbf{x} is the sum of a deterministic component $\mathbf{h}(\boldsymbol{\theta})$ (hereafter identified with the strain of the GW projected on the detector) and a stochastic component \mathbf{n} (the noise of the detector), $\mathbf{x}(\boldsymbol{\theta}) = \mathbf{h}(\boldsymbol{\theta}) + \mathbf{n}$. It is assumed that one can generate $\mathbf{h}(\boldsymbol{\theta})$ through a numerical process, so as to prepare a training set of ordered couples $\{\boldsymbol{\theta}_i, \mathbf{x}_i\}$ to train the density estimator.

The training process maximises the likelihood $\prod_i q_\phi(\boldsymbol{\theta}_i|\mathbf{x}_i)$ with respect to the model parameters ϕ . As shown in [55], the estimator converges to the true posterior density asymptotically with the dimension of the training set. A particular class of estimators called normalizing flows [58] has become increasingly popular for SNPE. In the following, we model the estimator as a neural spline flow (NSF), a spline-based neural normalizing flow [35, 59]. We use the implementation from the `sbi` package [60] — see also Appendix A for implementational details.

Once trained, the model q_ϕ can be sampled from in a fraction of a second, returning fast posterior samples $\{\boldsymbol{\theta}_n\}$. Moreover, differently from Markov-chain methods, the model can also be evaluated and returns fast accurate estimates of $p(\boldsymbol{\theta}|\mathbf{x})$.

The word “sequential” refers to the fact that the approximate density estimator $q_\phi(\boldsymbol{\theta}|\mathbf{x})$ targets a particular observation \mathbf{x}_o , as opposed to an amortized NPE which targets the entire prior volume of the training set. Specifically, sequential training proceeds through a series of adaptive steps, or rounds: at each round, new training samples are drawn from a proposal distribution $\tilde{p}(\boldsymbol{\theta})$, which is initially set to the prior $p(\boldsymbol{\theta})$ and then it shrinks adaptively at each round to prioritize samples with high posterior density $q_\phi(\boldsymbol{\theta}|\mathbf{x})$ conditioned to $\mathbf{x} = \mathbf{x}_o$. While the original implementation of SNPE in [55] proposes to draw the new samples directly from the posterior of

the previous round, we opt for a refined version called truncated SNPE (TSNPE) [57], as we observed it to give more stable results. We briefly summarize it here:

1. During the first round $r = 1$, the training samples $\{\boldsymbol{\theta}_i, \mathbf{x}_i\}_{r=1}$ are drawn from the prior $p(\boldsymbol{\theta})$ and the model is optimized with respect to $\{\boldsymbol{\theta}_i, \mathbf{x}_i\}_{r=1}$.
2. During the k -th round ($k > 1$), new training samples are still drawn from the prior $p(\boldsymbol{\theta})$, but they are rejected if they fall outside the $1 - \epsilon$ highest posterior density (HPD) region of $q_\phi(\boldsymbol{\theta}|\mathbf{x})$ from the previous round, evaluated at $\mathbf{x} = \mathbf{x}_o$. The model from the previous round $r = k - 1$ is then further optimized with respect to the collection of samples from all rounds $\{\boldsymbol{\theta}_i, \mathbf{x}_i\}_{r=1} \cup \dots \cup \{\boldsymbol{\theta}_i, \mathbf{x}_i\}_{r=k}$.
3. The training proceeds until a stopping criterion is met.

Here, ϵ is an hyperparameter that is fixed in advance and plays a crucial role: a large ϵ leads to undercovered posteriors due to large truncation of the original prior volume, while a small ϵ does not adapt the prior enough to advance the training. Reference [57] reports that the range $10^{-5} < \epsilon < 10^{-2}$ is working for a variety of benchmarking problems. In this work, we fix $\epsilon = 10^{-4}$ as we found it to give the best results.

To avoid overfitting, we stop the training when the truncated volume at the current round encompasses more than 80% of the truncated volume at the previous round. Moreover, at rounds $r > 1$, we also discard simulations from the first round since they are less informative.

More details about the data preparation and the density estimator are provided in Appendix A.

III. RINGDOWN WAVEFORM

The GW strain that we use for the inference has the form

$$\mathbf{h}(\boldsymbol{\theta}) = F_+ h_+ + F_\times h_\times \quad (1)$$

where F_+ and F_\times are the pattern functions of the detector [61], depending on the sky position and relative orientation of the source, of the polarization of the waveform and of the starting time of the ringdown. The plus- and cross-waveform components are expressed as superpositions of damped sinusoids as

$$h_+ = \sum_{l,m,n} \mathcal{A}_{lmn} e^{-\frac{(t-t_{\text{start}})}{\tau_{lmn}}} \cos(\Phi_{lmn}) Y_{lm}^+(\iota) \quad (2a)$$

$$h_\times = \sum_{l,m,n} \mathcal{A}_{lmn} e^{-\frac{(t-t_{\text{start}})}{\tau_{lmn}}} \sin(\Phi_{lmn}) Y_{lm}^\times(\iota) \quad (2b)$$

where $l \geq 2$, $|m| \leq l$ and $n \geq 0$, and

$$\Phi_{lmn} \equiv 2\pi f_{lmn}(t - t_{\text{start}}) + \phi_{lmn}. \quad (3)$$

The discrete indices (l, m, n) label the (complex) QNMs $\tilde{\omega}_{lmn} = 2\pi f_{lmn} + i/\tau_{lmn}$ of the remnant black hole, with f_{lmn} and τ_{lmn} being the (l, m, n) frequency and damping time, respectively. While the QNM indices (l, m, n) span a countably infinite set, numerical simulations show that only a finite subset is significantly excited in the aftermath of a binary black-hole merger [13, 14, 44]. The amplitudes \mathcal{A}_{lmn} quantify the extent to which different QNMs are excited [14, 22, 44, 62–65].

The expressions (2a) assume nonprecessing progenitors, implying the equatorial symmetry

$$\mathcal{A}_{l-mn} e^{i\phi_{l-mn}} = (-1)^l \mathcal{A}_{lmn} e^{-i\phi_{lmn}}. \quad (4)$$

Together with the symmetry $\tilde{\omega}_{l-mn} = -\tilde{\omega}_{lmn}^*$ valid for the QNMs of Kerr BHs, it allows us to reabsorb negative- m modes into positive- m ones and to restrict the sums over $m > 0$ only.

The plus- and cross- spherical harmonics are functions of the inclination angle ι defined as

$$Y_{lm}^{+, \times}(\iota) = {}_{-2}Y_{lm}(\iota, 0) \pm (-1)^l {}_{-2}Y_{l-m}(\iota, 0) \quad (5)$$

in terms of the spin-weighted spherical harmonics ${}_{-2}Y_{lm}$. Note that we set the azimuthal angle to zero because it is degenerate with the QNM phases. We also take the the spin-weighted spherical harmonics ${}_{-2}Y_{lm}$ to approximate the spin-weighted spheroidal harmonics [66], ${}_{-2}Y_{lm} \approx {}_{-2}S_{lmn}$.

For the parameter estimation, we follow [17, 67, 68] and keep sky position, polarization, starting time and inclination as fixed parameters.

As a consequence, the space of independent model parameters is spanned by $\boldsymbol{\theta} = \{M, \chi\} \cup \{\mathcal{A}_{lmn}, \phi_{lmn}\}_{lmn}$ and has $2(1 + N_{\text{modes}})$ dimensions. We assume that GR is valid and we map $\{M_f, \chi_f\}$ into the Kerr QNMs using the fits in [45].

IV. SIMULATED INJECTIONS

We perform simulated injections into zero noise [69, 70] to benchmark the ability to recover a known set of injected parameters. We simulate three systems:

1. **Kerr₂₂₀**: A system containing only the $(2, 2, 0)$ mode. This system is designed to benchmark our inference strategy on the simplest problem of a single excited mode.
2. **Kerr₂₂₁**: A system containing the $(2, 2, 0)$ mode and the $(2, 2, 1)$ mode, checking the ability to recover the fundamental tone and its first overtone.
3. **Kerr₃₃₀**: A system containing the $(2, 2, 0)$ and the $(3, 3, 0)$ mode, checking the ability to recover the fundamental tone and a higher angular mode.

In all cases, the mass and spin of the remnant BH are fixed to $M_f = 67 M_\odot$ and $\chi_f = 0.67$. The other

| Kerr ₂₂₀ : (2, 2, 0) | | | | | | | |
|---------------------------------|----------|---------------------|--|--------------|--|---------|-----|
| M_f | χ_f | \mathcal{A}_{220} | | ϕ_{220} | | ι | SNR |
| 67 M_\odot | 0.67 | 5 | | 1.047 | | π | 14 |

| Kerr ₂₂₁ : (2, 2, 0) + (2, 2, 1) | | | | | | | |
|---------------------------------------------|----------|---------------------|---------------------|--------------|--------------|---------|-----|
| M_f | χ_f | \mathcal{A}_{220} | \mathcal{A}_{221} | ϕ_{220} | ϕ_{221} | ι | SNR |
| 67 M_\odot | 0.67 | 8.92 | 9.81 | 1.047 | 4.19 | π | 14 |

| Kerr ₃₃₀ : (2, 2, 0) + (3, 3, 0) | | | | | | | |
|---------------------------------------------|----------|---------------------|---------------------|--------------|--------------|---------|-----|
| M_f | χ_f | \mathcal{A}_{220} | \mathcal{A}_{330} | ϕ_{220} | ϕ_{330} | ι | SNR |
| 67 M_\odot | 0.67 | 30 | 3 | 1.047 | 5.014 | $\pi/4$ | 53 |

TABLE I. Parameters of the simulated zero-noise injections. Amplitudes are expressed in units of 10^{-21} .

parameters are listed in Table I. For the Kerr₂₂₀ and the Kerr₂₂₁ systems, we fix the inclination angle to the GW150914-like value $\iota = \pi$ [67, 68]. Since the spherical harmonics $Y_{330}^{+, \times}$ vanish at $\iota = \pi$, we fix $\iota = \pi/4$ for the Kerr₃₃₀ system, in order to excite the higher angular mode.

Following [67], we fix the right ascension α , declination δ and polarization ψ to the GW150914-like values $\{\alpha, \delta, \psi\} = \{1.95, -1.27, 0.82\}$. Similarly, we fix the starting time of the ringdown to the median peak time estimated from the posterior samples of GW150914 [68, 71]; specifically, we fix the GPS starting time at H1 to be $t_{\text{H1}} = 1126259462.42323$, while the starting time at L1 is derived from the time delay from H1 using the sky location fixed above.

The SNRs are computed from the noise power spectral density (PSD), estimated from the data segments in the vicinity of the event GW150914 [53]. The amplitudes of Kerr₂₂₀ and the Kerr₂₂₁ systems are adjusted to give a signal-to-noise ratio $\text{SNR} \approx 14$, comparable to the SNRs of ringdown events observed so far, e.g., GW150914. On the other hand, $\text{SNR} \approx 14$ is too low to allow for a detection of the subdominant $(3, 3, 0)$ mode: following [14, 23], we expect that the higher mode $(3, 3, 0)$ is resolved from the $(2, 2, 0)$ starting from a ringdown SNR of $\mathcal{O}(50)$, for nonspinning progenitors with mass ratio $q \approx 1.5$. Therefore, we fix the corresponding amplitudes to $\{\mathcal{A}_{220}, \mathcal{A}_{330}\} = \{30 \times 10^{-21}, 3 \times 10^{-21}\}$, which results into $\text{SNR} \approx 53$.

We infer the posteriors from box-uniform priors in the model parameters, within the prior ranges listed in Table II. We benchmark our results against posterior samples obtained with the time-domain inference software **pyRing** (v2.3.0) [3, 52, 67, 72]. We sample with the nested sampler **cpnest** [73], using 4096 live points and 4094 maximum Markov-chain steps, which typically results in $\sim 20\text{k}$ posterior samples. For consistency, we extract 20k posterior samples from the trained estimator $q_\phi(\boldsymbol{\theta}|\mathbf{x}_o)$ when doing the comparisons.

We train the posterior density estimators on a single GPU A100. Individual training processes take $\{291, 324, 249\}$ epochs and last $\{81, 70, 52\}$ mins for the $\{\text{Kerr}_{220}, \text{Kerr}_{221}, \text{Kerr}_{330}\}$ models respectively. Figure

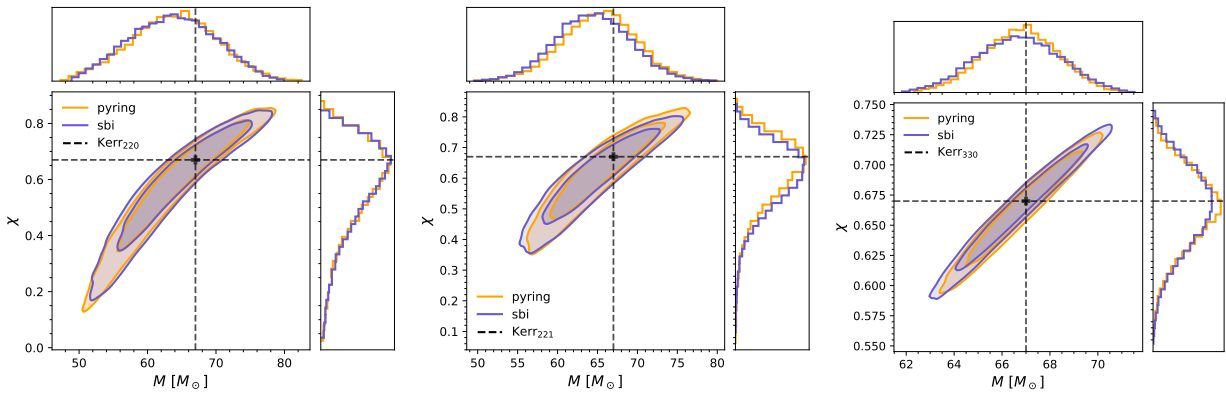


FIG. 1. Marginalized posteriors for (M_f, χ_f) for the three injected systems. The systems Kerr₂₂₀ and Kerr₂₂₁ have $\text{SNR} \approx 14$ while the system Kerr₃₃₀ has $\text{SNR} \approx 53$, which justifies its narrower posteriors. 2-D contours denote 68% and 90% credible regions. Black dashed lines denote the injected parameters.

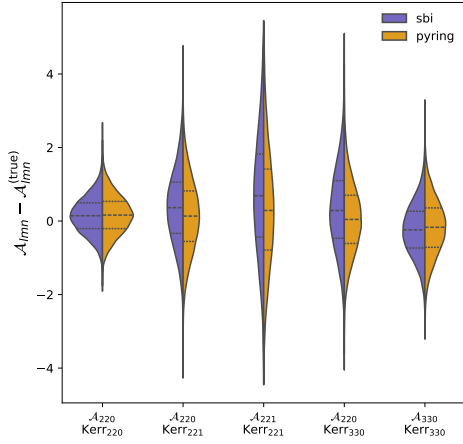


FIG. 2. Violin plots of the recovered amplitudes \mathcal{A}_{lmn} for each injected model. We subtract the injected values $\mathcal{A}_{lmn}^{(\text{true})}$ for better visualization. All amplitudes are expressed in units of 10^{-21} .

| Parameter | Prior range |
|---------------------|-----------------------------|
| M_f | $[20, 300] M_\odot$ |
| χ_f | $[0, 0.99]$ |
| \mathcal{A}_{220} | $[0.1, 50] \times 10^{-21}$ |
| \mathcal{A}_{221} | $[0, 50] \times 10^{-21}$ |
| \mathcal{A}_{330} | $[0, 50] \times 10^{-21}$ |
| ϕ_{lmn} | $[0, 2\pi]$ |

TABLE II. Prior ranges for inferring the model parameters. All priors are box-uniform distributions within the specified ranges.

1 displays the marginalized posteriors for (M_f, χ_f) obtained with `pyRing` and with our SBI approach, showing an excellent agreement between the two methods. Figure 2 shows that amplitudes, containing the physical information on the degree of excitation of the QNMs, are recovered consistently with Markov-chain methods for all injected systems. We also display full corner plots for the

Kerr₂₂₁ and Kerr₃₃₀ in Appendix C.

As an internal diagnostics, we perform coverage tests [74–76]. In particular we check that, over a set of simulated injections from the restricted priors $\tilde{p}(\theta)$, the Bayesian credible intervals can be used similar to frequentist confidence regions; equivalently, that the true injected values fall within the $\gamma\%$ credible regions in a fraction γ of the injections. This is a necessary condition for the density estimators to provide a consistent parameter estimation. Further details are provided in Appendix B. Figure 3 displays the cumulative distribution c.d.f. (γ) of the Bayesian credible intervals for the model Kerr₂₂₀: in order to check consistency with the identity, we evaluate c.d.f. (γ) for 100 catalogs, each consisting of 100 events. We see that c.d.f. (γ) has support well within the expected 90% credible interval around the diagonal line, represented by the gray region [4]¹. We obtain similar consistency results for the Kerr₂₂₁ and Kerr₃₃₀ models, as displayed in Appendix B.

Our results show that the time-domain SBI inference for ringdown returns posterior parameter predictions that are internally consistent and it reproduces the results obtained by the established Markov-chain methods.

V. INFERENCE OF REAL DATA

We perform a Bayesian parameter estimation on the real event GW150914 [1]. A full inspiral-merger-ringdown (IMR) analysis identified it as a binary BH with detector-frame total mass $M = 72^{+4}_{-3} M_\odot$ and binary mass ratio $q < 1.42$ at 90% credibility, while being compatible with vanishing progenitor spins [71]. In order to reconstruct

¹ Note that such tests are difficult with ordinary Markov-chain methods, in which typically the densities are sampled from but not evaluated exactly, often restricting the scope of coverage diagnostics to the marginalized 1-d distributions [77].

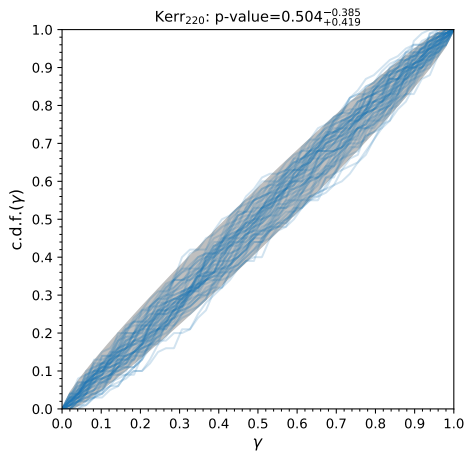


FIG. 3. Cumulative distribution of the coverage $\gamma(\theta_*, \mathbf{x}_*)$ for the injected model Kerr_{220} . Each of the 100 blue lines corresponds to the c.d.f. of γ from $N_s = 100$ draws of θ_* . The shaded gray area denotes the 90% uncertainty over c.d.f.(γ). We also quote the median and 90% confidence bounds of the KS test p-values across all draws.

the remnant properties, we analyze the event at $t_{\text{H1}} + 3$ ms, corresponding to $\sim 10M$ after the merger ($t_{\text{start}} \sim t_{\text{peak}} + 10M$ was found to mark the onset of the ringdown stage from the analysis of nearly equal mass NR simulations [44, 78]). This choice results in a ringdown-only SNR ~ 8.5 [54]. As in [67], we fix $\{\alpha, \delta, \phi\} = \{1.95, -1.27, 0.82\}$ and $\iota = \pi$. We assume a model containing only the fundamental mode (2, 2, 0), which dominates the late ringdown stage for nearly equal-mass nonspinning binaries [22, 44, 62, 79]. The training takes 282 epochs and lasts 91 minutes. Figure 4 shows the 90% credible regions of the reconstructed final mass and final spin using our SBI implementation, compared to the estimates from the `pyRing` software. The two results are in good agreement with each other. In the plot, we also display the final mass and spin deduced from the IMR posterior samples [71] using the phenomenological fits in [80, 81].

VI. CONCLUSIONS AND OUTLOOK

Our study shows that simulation-based GW inference of BBH ringdowns gives results that are both internally consistent and compatible with Markov-chain methods. After benchmarking SBI on a control set of injections at zero noise, we applied our methods to the analysis of real GW data from LIGO detectors. We see that inferences done using our model on the event GW150914 agrees with the inference of the traditional setup. It is important to note that zero-noise injections include several simplifications, but real data present noise and a morphological bias between the template and the underlying signal. The fact that our results are consistent in both cases constitutes a robust demonstration of the feasibility of our approach.

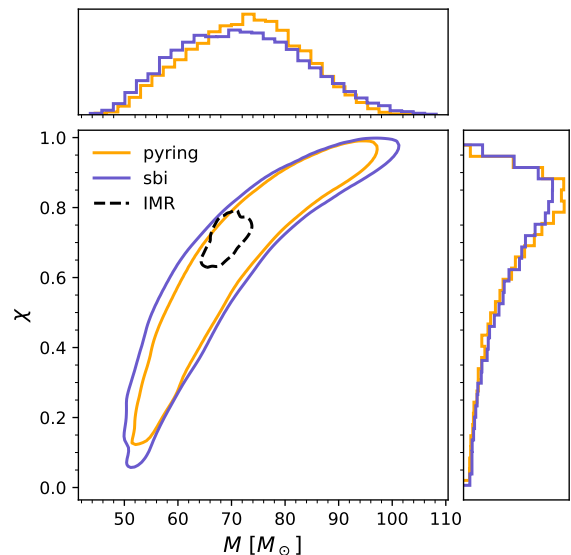


FIG. 4. Remnant properties of GW150914, obtained by analyzing the publicly released data from LVK [82]. Solid lines denote the 90% credible regions reconstructed with our SBI implementation (blue) and with the `pyRing` analysis (orange). We also display the final mass and spin obtained from the full IMR posterior samples [71] through the phenomenological remnant fits in [80, 81].

We envisage a number of future studies to further expand our results. First, a detailed investigation of all the promising ringdown events from the GW observations is ongoing. While the significance for detecting a second mode in present ringdown data is still debated [3, 4, 48, 68, 83, 84], there is tentative evidence that GW150914 and GW190521 [85] allow us to measure the presence of a subdominant overtone [67, 86] and of a higher angular harmonic [17, 18], respectively. We seek to confirm or refute these findings with our independent, likelihood-free method.

A promising application leverages on the ability of SBI to automatically marginalize over nuisance parameters. In particular, when inferring on ringdown signals, one is only interested in the small subset of modes which are better resolved. The presence of multiple modes, which are challenging to resolve individually, is a potential source of confusion noise and therefore it must be modeled. Moreover, an ideal model would allow for a variable number of such modes, in order to fit the residuals with greater flexibility. This problem is especially suited for SBI, as a variable number of background modes can be regarded as a collection of nuisances, and we will present a dedicated exploration in a follow-up work.

Lastly, we use sequential (i.e., nonamortised) NPE because it is convenient for analyzing individual observations, which is the scope of our work. On the other hand, amortized NPE might prove useful when assessing the expected performances of a detector on large population catalogs. Such studies are well timed, given the recent

adoption of the LISA mission [19] by the European Space Agency, and the strong efforts to build next-generation ground-based GW detectors [20, 21]. Relevant examples include [87] exploring a battery of diverse science cases, and [23, 25, 26, 88, 89] with a focus on BH spectroscopy. Since performing rigorous Bayesian analysis on tens of thousands of sources is computationally challenging, all these works approximate individual posterior densities with Fisher matrices, which are known to introduce systematic biases in the shape of the posterior recovery [90]. Training an amortized density estimator on the expected noise spectral densities would allow to drop such approximations and to draw much more robust conclusions.

VII. ACKNOWLEDGMENTS

We are especially grateful to Enrico Barausse and Marco Crisostomi for fruitful exchanges during an earlier stage of this work. CP thanks Elliot Finch for useful discussions. C.P. is supported by ERC Starting Grant No. 945155–GWmining, Cariplo Foundation Grant No. 2021-0555, MUR PRIN Grant No. 2022-Z9X4XS, and the ICSC National Research Centre funded by NextGenerationEU. CP acknowledges support from the European Union’s H2020 ERC Consolidator Grant “GRavity from Astrophysical to Microscopic Scales” (Grant No. GRAMS-815673) during a visit to SISSA. S.B. is supported by UKRI Stephen Hawking Fellowship No. EP/W005727. R.C. is supported by NSF Grants No. AST-2006538, PHY-2207502, PHY-090003 and PHY-20043, and by NASA Grants No. 20-LPS20-0011 and 21-ATP21-0010. Computational work was performed on the LEONARDO HPC facility hosted at CINECA, with allocations through INFN and Bicocca.

Software. We used the following public software: `scipy` [91] and `pycbc` [41] to estimate the PSD and the correlation matrix from noisy time series; `sbi` [60] for simulation based inference; `pyRing` [72] for Markov-chain ringdown inferences; `numpy` [92], `matplotlib` [93] and `seaborn` [94] for chain visualizations.

Appendix A: Technical details

In this Appendix, we provide technical details on the process of data preparation, and on the numerical implementation and training of the neural density estimator.

1. Data preparation

When performing simulated injections, we sample the strains at 2048 Hz and truncate them at a duration of 0.1 s, thus resulting in a data segment of 204 bins per detector. When analyzing real data, we use the publicly available data from GWOSC [82] at 4096 Hz and down-sample them to 2048 Hz.

We whiten the data directly in the time domain following [53],

$$h_{\text{white}}^a(\boldsymbol{\theta}) = \sum_b (L^{-1})^a_b h^b(\boldsymbol{\theta}) \quad (\text{A1})$$

where the matrix L is the (upper-triangular) Cholesky factor of the covariance matrix. Specifically, we first compute the auto-correlation function (ACF) from the inverse-Fourier transform of the PSD, then, we compute the covariance matrix as the Toeplitz matrix of the ACF (see Eq.s (39)-(44) of [53]). Noise realizations can be added to the whitened ringdown strain as simply as

$$\mathbf{x}_{\text{white}}(\boldsymbol{\theta}) = \mathbf{h}_{\text{white}}(\boldsymbol{\theta}) + \mathcal{N}(0, 1). \quad (\text{A2})$$

2. Density estimator

We model the density estimator as a neural spline flow (NSF) [35, 58] and use the implementation from the `sbi` package [60]. The relevant hyper-parameters are listed in Table III. In particular, the NSF is a flow of 5 transforms and each hidden layer contains 150 units.

The NSF does not take $\mathbf{x}_{\text{white}}$ in input directly, but we apply an embedding network for dimensional reduction: the raw input is a concatenation of $\mathbf{x}_{\text{white}}$ from two detectors (LIGO-Hanford and LIGO-Livingstone), thus resulting into an input dimension of $204 + 204$ bins; they are then mapped into 128 bins by a fully connected neural network with two hidden layers consisting of 150 units. The output of the embedding network is fed into the NSF.

We train and validate the density estimator in batches of 512 samples. During the first round we generate 50k training samples, while at later rounds we generate 100k additional samples. We use the Adam optimizer with learning rate 0.001.

Since neural networks learn better from standardized and/or normalized data [95], we linearly rescale $\mathbf{x}_{\text{white}}$ to have zero mean and unit variance along the feature dimension [96], and we normalize the parameters $\boldsymbol{\theta}$ between 0 and 1.

Finally, we vary the noise realizations in (A2) at each training epoch to make the inference resilient to specific

| Neural spline flow | |
|---------------------------|------------------|
| num_blocks | 2 |
| hidden_features | 150 |
| num_transforms | 5 |
| num_bins | 10 |
| batch_norm | True |
| Embedding FC network | |
| input_dim | 408 |
| num_hidden_layers | 2 |
| hidden_dim | 150 |
| output_dim | 128 |
| Training hyper-parameters | |
| num_simulations | [50k, 100k, ...] |
| batch_size | 512 |
| learning_rate | 0.001 |
| validation_fraction | 0.1 |
| trunc_quantile ϵ | 10^{-4} |
| stopping_ratio | 0.8 |
| varying_noise | True |

TABLE III. Hyper-parameters for the architecture and training of the the density estimator.

noise realizations². Note that the original implementation of `sbi` does not allow to vary noise realizations between training epochs. We leverage on the flexibility of object-oriented programming to wrap the original SNPE implementation of `sbi` and we redefine its loss method, so as to resample the noise at each evaluation of the loss³.

Appendix B: Coverage Test

Given model parameters $\boldsymbol{\theta}_*$ and a corresponding model realization $\mathbf{x}_* = \mathbf{h}(\boldsymbol{\theta}_*) + \mathbf{n}$, we define the coverage $\gamma(\boldsymbol{\theta}_*, \mathbf{x}_*)$ as the approximate posterior probability contained within the highest posterior density (HPD) region which has $\boldsymbol{\theta}_*$ at its boundary,

$$\gamma(\boldsymbol{\theta}_*, \mathbf{x}_*) = \int d\boldsymbol{\theta} \, q_\phi(\boldsymbol{\theta}|\mathbf{x}_*) \mathbb{1}[q_\phi(\boldsymbol{\theta}|\mathbf{x}_*) > q_\phi(\boldsymbol{\theta}_*|\mathbf{x}_*)] \quad (\text{B1})$$

² To avoid confusion, we clarify the distinction between training rounds and training epochs. A training round is the training update of the density estimator at each truncation of the prior volume. A training epoch is a single feed-forward and back-propagation step of the training set into the network. Each training round consists of several-to-many training epochs, necessary to optimize the model at the current round.

³ Such a data-augmentation strategy is feasible, because sampling a standard normal in (A2) is a fast numerical operation and it does not impact on the training time. In cases where noise generation is computationally costly, one would opt for alternative data augmentations, e.g., preparing the training set offline with multiple copies of the same raw strains $\mathbf{h}(\boldsymbol{\theta})$ but different noise realizations. See [48] for an example of the last strategy.

where q_ϕ is the density estimator.

The integral (B1) can be evaluated efficiently via importance sampling as the expectation value

$$\gamma(\boldsymbol{\theta}_*, \mathbf{x}_*) \approx \mathbb{E}_{\boldsymbol{\theta} \sim q_\phi(\boldsymbol{\theta}|\mathbf{x}_*)} (\mathbb{1}[q_\phi(\boldsymbol{\theta}|\mathbf{x}_*) > q_\phi(\boldsymbol{\theta}_*|\mathbf{x}_*)]) \quad (\text{B2})$$

thanks to the fact that the neural density estimator is fast to sample and to evaluate. It can be shown [75, 76] that, if the density estimator $q_\phi(\boldsymbol{\theta}|\mathbf{x})$ approximates the true posterior $p(\boldsymbol{\theta}|\mathbf{x})$, then the coverage across the prior $p(\boldsymbol{\theta})$ is distributed uniformly within $[0, 1]$. The latter statement is equivalent to $\text{c.d.f.}(\gamma) \equiv \int_0^\gamma d\gamma' p(\gamma') = \gamma$ for each $\gamma \equiv \gamma(\boldsymbol{\theta}_*, \mathbf{x}_*)$ and $\boldsymbol{\theta}_* \sim p(\boldsymbol{\theta})$. This is a necessary condition for the density estimator to be a valid inference and we check for it.

Since we are performing truncated SNPE, we cannot sample the injected parameters from the original prior, $\boldsymbol{\theta}_* \sim p(\boldsymbol{\theta})$. Indeed, sequential training progressively truncates the prior volume as the training proceeds and the density estimator is only guaranteed to work on the final version of the truncated prior $\tilde{p}(\boldsymbol{\theta})$. Therefore, in the case of TNSPE, the prior for the Bayesian coverage test must correspond to the final truncated prior, $\boldsymbol{\theta}_* \sim \tilde{p}(\boldsymbol{\theta})$.

Figure 5 displays coverage diagnostics for the injected models corresponding to Kerr₂₂₁ and Kerr₃₃₀, complementing the diagnostics for the Kerr₂₂₀ presented in Figure 3 in the main text.

Appendix C: Additional corner plots

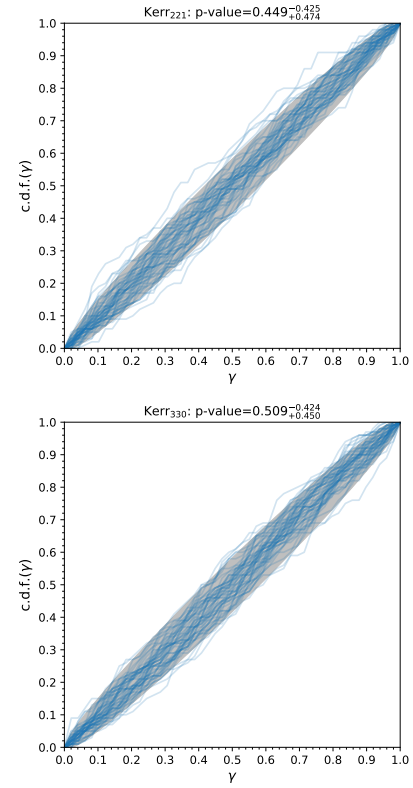


FIG. 5. Cumulative distributions of the coverage $\gamma(\boldsymbol{\theta}_*, \mathbf{x}_*)$ for the injected models Kerr₂₂₁ and Kerr₃₃₀. Each blue line corresponds to the c.d.f. of γ from $N_s = 100$ draws of $\boldsymbol{\theta}_*$. Each panel plots the cumulatives from 100 experiments. Shaded grey areas denote the 90% uncertainties over $\text{c.d.f.}(\gamma)$. For each panel, we also quote the median and 90% confidence bounds of the KS test p-values across all draws.

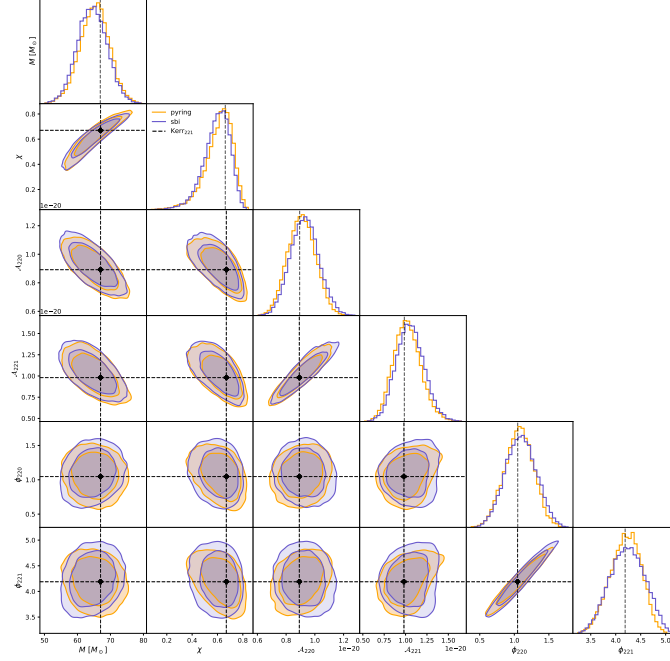


FIG. 6. Full corner plot of the posterior recovered from the injected system Kerr_{221} . 2-D contours denote the 68% and 90% credible regions. Black dashed lines denote the injected parameters from Table I.

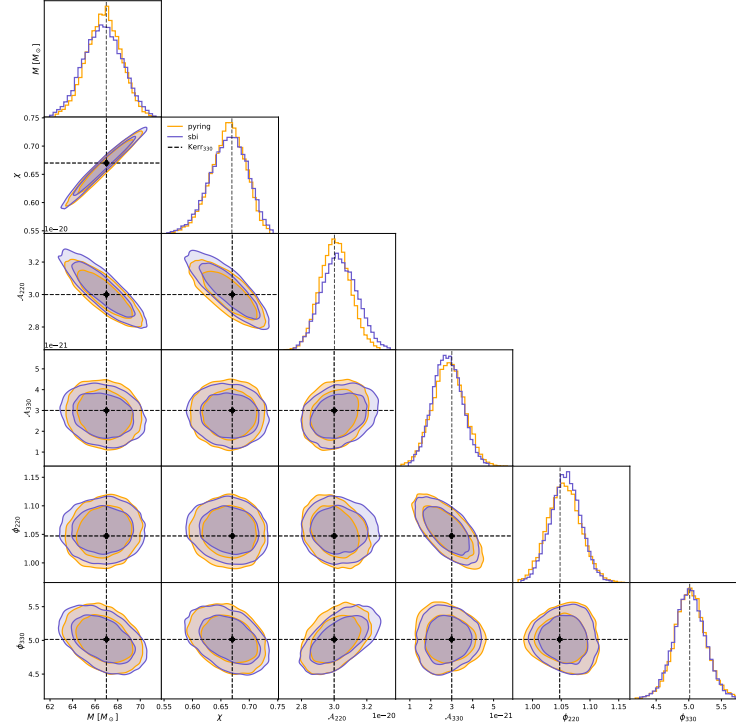


FIG. 7. Full corner plot of the posterior recovered from the injected system Kerr_{330} . 2-D contours denote the 68% and 90% credible regions. Black dashed lines denote the injected parameters from Table I.

-
- [1] B. P. Abbott *et al.* (LIGO Scientific, Virgo), *Phys. Rev. Lett.* **116**, 061102 (2016), [arXiv:1602.03837 \[gr-qc\]](#).
- [2] N. Yunes, K. Yagi, and F. Pretorius, *Phys. Rev. D* **94**, 084002 (2016), [arXiv:1603.08955 \[gr-qc\]](#).
- [3] R. Abbott *et al.* (LIGO Scientific, Virgo), *Phys. Rev. D* **103**, 122002 (2021), [arXiv:2010.14529 \[gr-qc\]](#).
- [4] R. Abbott *et al.* (LIGO Scientific, VIRGO, KAGRA), (2021), [arXiv:2112.06861 \[gr-qc\]](#).
- [5] R. P. Kerr, *Phys. Rev. Lett.* **11**, 237 (1963).
- [6] W. Israel, *Commun. Math. Phys.* **8**, 245 (1968).
- [7] B. Carter, *Phys. Rev. Lett.* **26**, 331 (1971).
- [8] S. A. Teukolsky, *Class. Quant. Grav.* **32**, 124006 (2015), [arXiv:1410.2130 \[gr-qc\]](#).
- [9] C. V. Vishveshwara, *Nature* **227**, 936 (1970).
- [10] K. D. Kokkotas and B. G. Schmidt, *Living Rev. Rel.* **2**, 2 (1999), [arXiv:gr-qc/9909058](#).
- [11] E. Berti, V. Cardoso, and A. O. Starinets, *Class. Quant. Grav.* **26**, 163001 (2009), [arXiv:0905.2975 \[gr-qc\]](#).
- [12] S. A. Teukolsky, *Phys. Rev. Lett.* **29**, 1114 (1972).
- [13] E. Berti, V. Cardoso, and C. M. Will, *Phys. Rev. D* **73**, 064030 (2006), [arXiv:gr-qc/0512160](#).
- [14] E. Berti, J. Cardoso, V. Cardoso, and M. Cavaglia, *Phys. Rev. D* **76**, 104044 (2007), [arXiv:0707.1202 \[gr-qc\]](#).
- [15] O. Dreyer, B. J. Kelly, B. Krishnan, L. S. Finn, D. Garrison, and R. Lopez-Aleman, *Class. Quant. Grav.* **21**, 787 (2004), [arXiv:gr-qc/0309007](#).
- [16] E. Barausse and T. P. Sotiriou, *Phys. Rev. Lett.* **101**, 099001 (2008), [arXiv:0803.3433 \[gr-qc\]](#).
- [17] C. D. Capano, M. Cabero, J. Westerweck, J. Abedi, S. Kasta, A. H. Nitz, Y.-F. Wang, A. B. Nielsen, and B. Krishnan, *Phys. Rev. Lett.* **131**, 221402 (2023), [arXiv:2105.05238 \[gr-qc\]](#).
- [18] H. Siegel, M. Isi, and W. M. Farr, *Phys. Rev. D* **108**, 064008 (2023), [arXiv:2307.11975 \[gr-qc\]](#).
- [19] P. Amaro-Seoane, H. Audley, S. Babak, J. Baker, E. Barausse, P. Bender, E. Berti, P. Binetruy, M. Born, D. Bortoluzzi, J. Camp, C. Caprini, V. Cardoso, M. Colpi, J. Conklin, N. Cornish, C. Cutler, K. Danzmann, R. Dolesi, L. Ferraioli, V. Ferroni, E. Fitzsimons, J. Gair, L. Gesa Bote, D. Giardini, F. Gibert, C. Grimaldi, H. Halloin, G. Heinzel, T. Hertog, M. Hewitson, K. Holley-Bockelmann, D. Hollington, M. Hueller, H. Inchauspe, P. Jetzer, N. Karnesis, C. Killow, A. Klein, B. Klipstein, N. Korsakova, S. L. Larson, J. Livas, I. Lloro, N. Man, D. Mance, J. Martino, I. Mateos, K. McKenzie, S. T. McWilliams, C. Miller, G. Mueller, G. Nardini, G. Nelemans, M. Nofrarias, A. Petiteau, P. Pivato, E. Plagnol, E. Porter, J. Reiche, D. Robertson, N. Robertson, E. Rossi, G. Russano, B. Schutz, A. Sesana, D. Shoemaker, J. Slutsky, C. F. Sopuerta, T. Sumner, N. Tamanini, I. Thorpe, M. Tröbs, M. Vallisneri, A. Vecchio, D. Vetrugno, S. Vitale, M. Volonteri, G. Wanner, H. Ward, P. Wass, W. Weber, J. Ziemer, and P. Zweifel, [arXiv:1702.00786 \(2017\)](#), [arXiv:1702.00786 \[astro-ph.IM\]](#).
- [20] M. Punturo *et al.*, *Class. Quant. Grav.* **27**, 194002 (2010).
- [21] B. P. Abbott *et al.* (LIGO Scientific), *Class. Quant. Grav.* **34**, 044001 (2017), [arXiv:1607.08697 \[astro-ph.IM\]](#).
- [22] S. Gossan, J. Veitch, and B. S. Sathyaprakash, *Phys. Rev. D* **85**, 124056 (2012), [arXiv:1111.5819 \[gr-qc\]](#).
- [23] E. Berti, A. Sesana, E. Barausse, V. Cardoso, and K. Belczynski, *Phys. Rev. Lett.* **117**, 101102 (2016), [arXiv:1605.09286 \[gr-qc\]](#).
- [24] M. Cabero, J. Westerweck, C. D. Capano, S. Kumar, A. B. Nielsen, and B. Krishnan, *Phys. Rev. D* **101**, 064044 (2020), [arXiv:1911.01361 \[gr-qc\]](#).
- [25] S. Bhagwat, C. Pacilio, E. Barausse, and P. Pani, *Phys. Rev. D* **105**, 124063 (2022), [arXiv:2201.00023 \[gr-qc\]](#).
- [26] S. Bhagwat, C. Pacilio, P. Pani, and M. Mapelli, *Phys. Rev. D* **108**, 043019 (2023), [arXiv:2304.02283 \[gr-qc\]](#).
- [27] S. Kumar, A. H. Nitz, and X. J. Forteza, (2022), [arXiv:2202.12762 \[astro-ph.IM\]](#).
- [28] Q. Baghi, N. Korsakova, J. Slutsky, E. Castelli, N. Karnesis, and J.-B. Bayle, *Phys. Rev. D* **105**, 042002 (2022), [arXiv:2112.07490 \[gr-qc\]](#).
- [29] A. Spadaro, R. Buscicchio, D. Vetrugno, A. Klein, D. Gerosa, S. Vitale, R. Dolesi, W. J. Weber, and M. Colpi, *Phys. Rev. D* **108**, 123029 (2023), [arXiv:2306.03923 \[gr-qc\]](#).
- [30] A. Toubiana, L. Pompili, A. Buonanno, J. R. Gair, and M. L. Katz, (2023), [arXiv:2307.15086 \[gr-qc\]](#).
- [31] K. Cranmer, J. Brehmer, and G. Louppe, *Proceedings of the National Academy of Science* **117**, 30055 (2020), [arXiv:1911.01429 \[stat.ML\]](#).
- [32] A. J. K. Chua and M. Vallisneri, *Phys. Rev. Lett.* **124**, 041102 (2020), [arXiv:1909.05966 \[gr-qc\]](#).
- [33] H. Gabbard, C. Messenger, I. S. Heng, F. Tonolini, and R. Murray-Smith, *Nature Phys.* **18**, 112 (2022), [arXiv:1909.06296 \[astro-ph.IM\]](#).
- [34] S. R. Green, C. Simpson, and J. Gair, *Phys. Rev. D* **102**, 104057 (2020), [arXiv:2002.07656 \[astro-ph.IM\]](#).
- [35] S. R. Green and J. Gair, *Mach. Learn. Sci. Tech.* **2**, 03LT01 (2021), [arXiv:2008.03312 \[astro-ph.IM\]](#).
- [36] M. Dax, S. R. Green, J. Gair, J. H. Macke, A. Buonanno, and B. Schölkopf, *Phys. Rev. Lett.* **127**, 241103 (2021), [arXiv:2106.12594 \[gr-qc\]](#).
- [37] M. Dax, S. R. Green, J. Gair, M. Pürrer, J. Wildberger, J. H. Macke, A. Buonanno, and B. Schölkopf, *Phys. Rev. Lett.* **130**, 171403 (2023), [arXiv:2210.05686 \[gr-qc\]](#).
- [38] J. Wildberger, M. Dax, S. R. Green, J. Gair, M. Pürrer, J. H. Macke, A. Buonanno, and B. Schölkopf, *Phys. Rev. D* **107**, 084046 (2023), [arXiv:2211.08801 \[gr-qc\]](#).
- [39] U. Bhardwaj, J. Alvey, B. K. Miller, S. Nissanke, and C. Weniger, *Phys. Rev. D* **108**, 042004 (2023), [arXiv:2304.02035 \[gr-qc\]](#).
- [40] J. Veitch *et al.*, *Phys. Rev. D* **91**, 042003 (2015), [arXiv:1409.7215 \[gr-qc\]](#).
- [41] C. M. Biwer, C. D. Capano, S. De, M. Cabero, D. A. Brown, A. H. Nitz, and V. Raymond, *Publ. Astron. Soc. Pac.* **131**, 024503 (2019), [arXiv:1807.10312 \[astro-ph.IM\]](#).
- [42] G. Ashton and C. Talbot, *Mon. Not. Roy. Astron. Soc.* **507**, 2037 (2021), [arXiv:2106.08730 \[gr-qc\]](#).
- [43] G. Ashton *et al.*, *Nature* **2**, 10.1038/s43586-022-00121-x (2022), [arXiv:2205.15570 \[stat.CO\]](#).
- [44] L. London, D. Shoemaker, and J. Healy, *Phys. Rev. D* **90**, 124032 (2014), [Erratum: *Phys. Rev. D* **94**, 069902 (2016)], [arXiv:1404.3197 \[gr-qc\]](#).
- [45] L. London and E. Fauchon-Jones, *Class. Quant. Grav.* **36**, 235015 (2019), [arXiv:1810.03550 \[gr-qc\]](#).
- [46] V. Baibhav, M. H.-Y. Cheung, E. Berti, V. Cardoso, G. Carullo, R. Cotesta, W. Del Pozzo, and F. Duque, *Phys. Rev. D* **108**, 104020 (2023), [arXiv:2302.03050 \[gr-qc\]](#).

- [47] M. H.-Y. Cheung, E. Berti, V. Baibhav, and R. Cotesta, *Phys. Rev. D* **109**, 044069 (2024), [arXiv:2310.04489 \[gr-qc\]](#).
- [48] M. Crisostomi, K. Dey, E. Barausse, and R. Trotta, *Phys. Rev. D* **108**, 044029 (2023), [arXiv:2305.18528 \[gr-qc\]](#).
- [49] S. Bhagwat and C. Pacilio, *Phys. Rev. D* **104**, 024030 (2021), [arXiv:2101.07817 \[gr-qc\]](#).
- [50] D. P. Kingma and M. Welling, *arXiv e-prints*, [arXiv:1312.6114 \(2013\)](#), [arXiv:1312.6114 \[stat.ML\]](#).
- [51] C. Doersch, *arXiv e-prints*, [arXiv:1606.05908 \(2016\)](#), [arXiv:1606.05908 \[stat.ML\]](#).
- [52] G. Carullo, W. Del Pozzo, and J. Veitch, *Phys. Rev. D* **99**, 123029 (2019), [Erratum: *Phys. Rev. D* **100**, 089903 (2019)], [arXiv:1902.07527 \[gr-qc\]](#).
- [53] M. Isi and W. M. Farr, (2021), [arXiv:2107.05609 \[gr-qc\]](#).
- [54] B. P. Abbott *et al.* (LIGO Scientific, Virgo), *Phys. Rev. Lett.* **116**, 221101 (2016), [Erratum: *Phys. Rev. Lett.* **121**, 129902 (2018)], [arXiv:1602.03841 \[gr-qc\]](#).
- [55] G. Papamakarios and I. Murray, *Advances in neural information processing systems* **29** (2016), [arXiv:1605.06376 \[stat.ML\]](#).
- [56] D. Greenberg, M. Nonnenmacher, and J. Macke, in *International Conference on Machine Learning* (PMLR, 2019) pp. 2404–2414, [arXiv:1905.07488 \[cs.LG\]](#).
- [57] M. Deistler, P. J. Goncalves, and J. H. Macke, *Advances in Neural Information Processing Systems* **35**, 23135 (2022), [arXiv:2210.04815 \[stat.ML\]](#).
- [58] G. Papamakarios, E. Nalisnick, D. J. Rezende, S. Mohamed, and B. Lakshminarayanan, *Normalizing flows for probabilistic modeling and inference* (2021), [arXiv:1912.02762 \[stat.ML\]](#).
- [59] C. Durkan, A. Bekasov, I. Murray, and G. Papamakarios, *arXiv e-prints*, [arXiv:1906.04032 \(2019\)](#), [arXiv:1906.04032 \[stat.ML\]](#).
- [60] A. Tejero-Cantero, J. Boelts, M. Deistler, J.-M. Lueckmann, C. Durkan, P. J. Goncalves, D. S. Greenberg, and J. H. Macke, *Journal of Open Source Software* **5**, 2505 (2020).
- [61] P. Jaranowski, A. Krolak, and B. F. Schutz, *Phys. Rev. D* **58**, 063001 (1998), [arXiv:gr-qc/9804014](#).
- [62] I. Kamaretsos, M. Hannam, and B. Sathyaprakash, *Phys. Rev. Lett.* **109**, 141102 (2012), [arXiv:1207.0399 \[gr-qc\]](#).
- [63] L. T. London, *Phys. Rev. D* **102**, 084052 (2020), [arXiv:1801.08208 \[gr-qc\]](#).
- [64] X. Jiménez Forteza, S. Bhagwat, P. Pani, and V. Ferrari, *Phys. Rev. D* **102**, 044053 (2020), [arXiv:2005.03260 \[gr-qc\]](#).
- [65] X. J. Forteza, S. Bhagwat, S. Kumar, and P. Pani, *Phys. Rev. Lett.* **130**, 021001 (2023), [arXiv:2205.14910 \[gr-qc\]](#).
- [66] E. Berti and A. Klein, *Phys. Rev. D* **90**, 064012 (2014), [arXiv:1408.1860 \[gr-qc\]](#).
- [67] M. Isi, M. Giesler, W. M. Farr, M. A. Scheel, and S. A. Teukolsky, *Phys. Rev. Lett.* **123**, 111102 (2019), [arXiv:1905.00869 \[gr-qc\]](#).
- [68] R. Cotesta, G. Carullo, E. Berti, and V. Cardoso, *Phys. Rev. Lett.* **129**, 111102 (2022), [arXiv:2201.00822 \[gr-qc\]](#).
- [69] S. Nissanke, D. E. Holz, S. A. Hughes, N. Dalal, and J. L. Sievers, *Astrophys. J.* **725**, 496 (2010), [arXiv:0904.1017 \[astro-ph.CO\]](#).
- [70] C. L. Rodriguez, B. Farr, V. Raymond, W. M. Farr, T. B. Littenberg, D. Fazi, and V. Kalogera, *Astrophys. J.* **784**, 119 (2014), [arXiv:1309.3273 \[astro-ph.HE\]](#).
- [71] <https://dcc.ligo.org/ligo-p1800370/public> (2022).
- [72] G. Carullo, W. Del Pozzo, and J. Veitch, *pyRing*: a time-domain ringdown analysis python package, git.ligo.org/lscsoft/pyring (2023).
- [73] <https://johnveitch.github.io/cpnest/>.
- [74] S. R. Cook, A. Gelman, and D. B. Rubin, *Journal of Computational and Graphical Statistics* **15**, 675 (2006).
- [75] S. Talts, M. Betancourt, D. Simpson, A. Vehtari, and A. Gelman, *arXiv e-prints*, [arXiv:1804.06788 \(2018\)](#), [arXiv:1804.06788 \[stat.ME\]](#).
- [76] K. Karchev, R. Trotta, and C. Weniger, *MNRAS* **510**, 1093 (2022), [arXiv:2209.06733 \[astro-ph.CO\]](#).
- [77] I. M. Romero-Shaw *et al.*, *Mon. Not. Roy. Astron. Soc.* **499**, 3295 (2020), [arXiv:2006.00714 \[astro-ph.IM\]](#).
- [78] S. Bhagwat, M. Okounkova, S. W. Ballmer, D. A. Brown, M. Giesler, M. A. Scheel, and S. A. Teukolsky, *Phys. Rev. D* **97**, 104065 (2018), [arXiv:1711.00926 \[gr-qc\]](#).
- [79] I. Kamaretsos, M. Hannam, S. Husa, and B. S. Sathyaprakash, *Phys. Rev. D* **85**, 024018 (2012), [arXiv:1107.0854 \[gr-qc\]](#).
- [80] E. Barausse, V. Morozova, and L. Rezzolla, *Astrophys. J.* **758**, 63 (2012), [Erratum: *Astrophys. J.* **786**, 76 (2014)], [arXiv:1206.3803 \[gr-qc\]](#).
- [81] F. Hofmann, E. Barausse, and L. Rezzolla, *Astrophys. J. Lett.* **825**, L19 (2016), [arXiv:1605.01938 \[gr-qc\]](#).
- [82] <https://gwosc.org/gwtc-1/> (2020).
- [83] R. Abbott *et al.* (LIGO Scientific, Virgo), *Astrophys. J. Lett.* **900**, L13 (2020), [arXiv:2009.01190 \[astro-ph.HE\]](#).
- [84] M. Isi and W. M. Farr, (2022), [arXiv:2202.02941 \[gr-qc\]](#).
- [85] R. Abbott *et al.* (LIGO Scientific, Virgo), *Phys. Rev. Lett.* **125**, 101102 (2020), [arXiv:2009.01075 \[gr-qc\]](#).
- [86] E. Finch and C. J. Moore, *Phys. Rev. D* **106**, 043005 (2022), [arXiv:2205.07809 \[gr-qc\]](#).
- [87] M. Branchesi *et al.*, *JCAP* **07**, 068, [arXiv:2303.15923 \[gr-qc\]](#).
- [88] A. Maselli, S. Yi, L. Pierini, V. Vellucci, L. Reali, L. Gualtieri, and E. Berti, *Phys. Rev. D* **109**, 064060 (2024), [arXiv:2311.14803 \[gr-qc\]](#).
- [89] S. Yi, A. Kuntz, E. Barausse, E. Berti, M. H.-Y. Cheung, K. Kritos, and A. Maselli, *Phys. Rev. D* **109**, 124029 (2024), [arXiv:2403.09767 \[gr-qc\]](#).
- [90] M. Vallisneri, *Phys. Rev. D* **77**, 042001 (2008), [arXiv:gr-qc/0703086](#).
- [91] P. Virtanen, R. Gommers, T. E. Oliphant, M. Haberland, T. Reddy, D. Cournapeau, E. Burovski, P. Peterson, W. Weckesser, J. Bright, S. J. van der Walt, M. Brett, J. Wilson, K. J. Millman, N. Mayorov, A. R. J. Nelson, E. Jones, R. Kern, E. Larson, C. J. Carey, Í. Polat, Y. Feng, E. W. Moore, J. VanderPlas, D. Laxalde, J. Perktold, R. Cimrman, I. Henriksen, E. A. Quintero, C. R. Harris, A. M. Archibald, A. H. Ribeiro, F. Pedregosa, P. van Mulbregt, and SciPy 1.0 Contributors, *Nature Methods* **17**, 261 (2020).
- [92] C. R. Harris, K. J. Millman, S. J. van der Walt, R. Gommers, P. Virtanen, D. Cournapeau, E. Wieser, J. Taylor, S. Berg, N. J. Smith, R. Kern, M. Picus, S. Hoyer, M. H. van Kerkwijk, M. Brett, A. Haldane, J. F. del Río, M. Wiebe, P. Peterson, P. Gérard-Marchant, K. Sheppard, T. Reddy, W. Weckesser, H. Abbasi, C. Gohlke, and T. E. Oliphant, *Nature* **585**, 357 (2020).
- [93] J. D. Hunter, *Computing in Science & Engineering* **9**, 90 (2007).
- [94] M. L. Waskom, *Journal of Open Source Software* **6**, 3021 (2021).
- [95] Y. LeCun, L. Bottou, G. B. Orr, and K. R. Müller, *Efficient backprop*, in *Neural Networks: Tricks of the Trade*,

edited by G. B. Orr and K.-R. Müller (Springer Berlin Heidelberg, Berlin, Heidelberg, 1998) pp. 9–50.

[96] D. George and E. A. Huerta, [Phys. Rev. D](#) **97**, 044039 (2018), [arXiv:1701.00008 \[astro-ph.IM\]](#).